



Quenched Galaxies are Important Host Candidates of Binary Black Hole and Binary Neutron Star Mergers

Xiaobo Gong^{1,2,3,4}, Feng-Hui Zhang^{1,2,4}, Xiaoyu Kang^{1,2,4}, and Lifang Li^{1,2,4}

¹ Yunnan Observatories, Chinese Academy of Sciences, Kunming 650216, China; gxbo@ynao.ac.cn

² Key Laboratory for the Structure and Evolution of Celestial Objects, Chinese Academy of Sciences, Kunming 650216, China

³ University of Chinese Academy of Sciences, Beijing 100049, China

⁴ International Centre of Supernovae, Yunnan Key Laboratory, Kunming 650216, China

Received 2023 April 21; revised 2023 May 29; accepted 2023 June 1; published 2023 July 26

Abstract

In this work, we present the probabilities of mergers of binary black holes (BBHs) and binary neutron stars (BNSs) as functions of stellar mass, metallicity, specific star formation rate (sSFR), and age for galaxies with redshift $z \leq 0.1$. Using the binary-star evolution (BSE) code and some fitting formulae, we construct a phenomenological model of cosmic gravitational wave (GW) merger events. By using the Bayesian analysis method and the observations from Advanced LIGO and Virgo, we obtain the relevant parameters of the phenomenological model (such as the maximum black hole mass is $93_{-22}^{+73} M_{\odot}$). Combining the above model results with the galaxy catalog given by the EMERGE empirical galaxy model, we find the normalized probability of occurrence of a merger event varying with $\log_{10}(\text{sSFR}/\text{yr}^{-1})$ for galaxies with $z \leq 0.1$ is different from that in previous studies, that is, two peaks exist in this work while there is only one peak ($\log_{10}(\text{sSFR}/\text{yr}^{-1}) = -10$) in the previous work. The sSFR value corresponding to the new peak is $\log_{10}(\text{sSFR}/\text{yr}^{-1}) = -12$ and in line with the value ($\log_{10}(\text{sSFR}/\text{yr}^{-1}) = -12.65_{-0.66}^{+0.44}$) of NGC 4493, the host galaxy of BNS merger event GW170817. The new peak is caused by today's quenched galaxies, which give a large contribution to the total SFR at high redshift in the EMERGE empirical galaxy model. Moreover, we find that the BNS mergers are most likely detected in galaxies with age ~ 11 Gyr, which is greater than previous results (6–8 Gyr) and close to the age of NGC 4993, $13.2_{-0.9}^{+0.5}$ Gyr.

Key words: stars: black holes – stars: massive – gravitational waves – galaxies: evolution

1. Introduction

The direct detection of gravitational waves (GWs) has opened a new era in astronomical observation. Since the first binary black hole (BBH) merger was detected by Advanced LIGO (Aasi et al. 2015) in 2015, many GW events associated with merging BBHs or binary neutron stars (BNSs) have been confirmed by Advanced LIGO and Advanced Virgo (Acernese et al. 2015; Abbott et al. 2021). In the future, the next-generation ground-based GW detectors will help us to reconstruct the redshift evolution of the BBH merger rate up to very high redshifts (Santoliquido et al. 2022). The observations will provide a rapidly growing sample of BBH and BNS systems. Up to now, 90 GW event candidates have been detected in the third gravitational wave transient catalog (GWTC-3), which includes 82 BBHs and 2 BNSs (Abbott et al. 2021). These observations have implied that heavy black holes (BHs) bigger than $30 M_{\odot}$ exist. But there is no conclusive evidence for BHs bigger than $20 M_{\odot}$ from X-ray binaries (Özel et al. 2010; Farr et al. 2011). These GW observations are helpful in understanding the evolution of massive stars and probing statistically the origins of BHs.

There exists two channels to form a BBH or BNS: an isolated massive binary via stellar evolution and a dense N -body stellar

system via dynamical interactions (such as globular clusters or nuclear clusters: Belczynski et al. 2018; Rastello et al. 2019). We just focus on isolated binary evolution in this work. For binary evolution, there exist major theoretical uncertainties, including core-collapse supernova (CCSN), common envelope (CE), and stellar wind. (i) The physics of a CCSN is remarkably complex, and the condition that a star directly collapses to form a BH has remained controversial up to now (Chan et al. 2018; Kuroda et al. 2018, 2022; Vartanyan et al. 2022). (ii) The CE phase plays an important role in the formation of compact binary mergers (Ricker & Taam 2008; Ivanova & Nandez 2016). However, the CE hydrodynamical simulations are very difficult due to the large ranges in timescales and length scales (Lau et al. 2022; Trani et al. 2022). (iii) Stellar wind is also crucial and it governs the final mass of a star before the supernova stage, but current stellar wind models cannot give an exact description (Vink & Sander 2021; Gormaz-Matamala et al. 2022). Therefore, models of rapid stellar evolution are usually used to simulate the formation of compact binary mergers. The models of rapid stellar evolution make use of a number of comprehensive analytic formulae that enable one to model the most complex binary physics process to record the history of binary evolution.

Apart from the above stellar evolution models, there exist some fitting formulae (about the BBH mass spectrum, the BBH mass-ratio distribution, the delay time distribution, the evolutions of star formation rate (SFR) density and metallicity, etc.) to help us to determine the cosmic compact binary mergers (Talbot & Thrane 2018). For example, Abbott et al. (2019a) have presented a power-law BBH mass spectrum with an index $\alpha = -1.3$. Littenberg et al. (2015), Kovetz et al. (2017), and Fishbach et al. (2020) gave a BBH mass spectrum with a mass gap between neutron star (NS) and BH. Detecting whether or not there exists a mass gap is helpful for constraining supernova physics and binary evolution (Fishbach et al. 2020). If an exact mass spectrum of BBH mergers is given, we can use it to constrain models of evolutionary population synthesis.

We need not only models of stellar evolution and of galaxy formation and evolution, but also observations of the host galaxies of merger events. However, BBH mergers are not expected to have electromagnetic counterparts. A BNS merger can lead to a short gamma-ray burst and trigger a kilonova, but there are only two BNS merger events (GW170817 and GW190425). For the second event, GW190425 (Abbott et al. 2020a), unfortunately, the electromagnetic emission signal is uncertain or nearly undetected (Boersma et al. 2021). The first BNS merger event, GW170817 (Abbott et al. 2017), is the only confirmed object with a simultaneous electromagnetic counterpart (Raaijmakers et al. 2021). Its electromagnetic emission ranges from gamma rays to radio bands. The host galaxy of GW170817 is NGC 4993. It is an S0 galaxy (Levan et al. 2017), its stellar mass is $4.46 \times 10^{10} M_{\odot}$, its specific star formation rate (sSFR) is $\log_{10}(\text{sSFR}/\text{yr}^{-1}) = -12.65_{-0.66}^{+0.44}$, its age is $13.2_{-0.9}^{+0.5}$ Gyr (Blanchard et al. 2017), and it probably has a weak active galactic nucleus (Blanchard et al. 2017; Levan et al. 2017; Palmese et al. 2017). It is very strange that a BNS merger happens in a galaxy with very low SFR. Mapelli et al. (2018), Artale et al. (2019, 2020), Jiang et al. (2020), and Chu et al. (2022) have used models of galaxy formation and evolutionary population synthesis to derive the cosmic merger rate of compact stars and study the properties of their host galaxies. Their results showed that the merger rate per galaxy is positively correlated with the SFR and stellar mass of the host galaxy. However, they used semianalytic models for the galaxy, the sSFR is relative large ($\log_{10}(\text{sSFR}/\text{yr}^{-1}) \sim -10$), and the age is small (6–8 Gyr). Therefore, in this paper we will use the EMERGE empirical galaxy model to study the properties for the host galaxies of BNS mergers.

The outline of this paper is as follows. In Section 2.1, we introduce the binary stellar evolution code and the calculation of binary population synthesis (BPS). In Section 2.2 we present the basic components of a phenomenological model for the cosmic GW merger events. In Section 2.3, in combination with the posterior sample of the observed GWTC-1 BBH merger event, we give the posterior of free parameters by the Bayesian

analysis method and the derived parameters in the phenomenological model. In Section 3.1, the empirical model of galaxy formation is introduced. In Section 3.2, we give the methods of calculating the galaxy’s age, metallicity, and the normalized probability of occurrence of a merger event. In Section 3.3, we show the probabilities of BBH and BNS mergers as functions of stellar mass, metallicity, sSFR, and age for galaxies with redshift $z \leq 0.1$. In Section 4, we discuss the influences of free parameters in our phenomenological model on the results. And in Section 5, we give a summary.

2. The Phenomenological Model of a Cosmic GW Merger Event

In order to constrain/obtain the free parameters in the cosmological model (Section 2.2), which will be used in the properties for the host galaxy of a merger event (Section 3), we need use the posterior mass and redshift sample for the observed LIGO/GWTC-1 BBH GW event and the model for the cosmic GW merger event. The construction of a model of the cosmic GW merger event needs the BBH merger sample in a stellar population (SP) and the evolutions of cosmic SFR density and metallicity with redshift (Section 2.2.4). If we use the BBH merger sample of an SP in the model and fitting calculation, the size of the data is too large and the calculation will be very time-consuming. Moreover, the BH formation and evolution are still not fully understood. Therefore, we will use the merger efficiency (Section 2.2.1), the mass spectrum of BBH mergers (Section 2.2.2), and the delay time (Section 2.2.3) rather than the BBH merger sample to construct the phenomenological model in this paper. The functional form and the coefficient range for the merger efficiency and the metallicity relation, and the coefficient range for the mass spectrum of BBH mergers, will be obtained by the binary-star evolution (BSE) code and BPS calculations (Section 2.1). Therefore, we will first introduce the BSE code and BPS method in Section 2.1, the basic components of the phenomenological model (merger efficiency, mass spectrum of BBH mergers, delay time, cosmological model, and evolutions of cosmic SFR density and mean metallicity with redshift) in Section 2.2, and the posterior of free parameters via the Bayesian method and the posterior sample for the LIGO/GWTC-1 BBH GW event, together with the derived free parameters of the cosmological model, in Section 2.3.

2.1. BSE and BPS

2.1.1. BSE

To obtain the functional form and coefficient range for the merge efficiency and the coefficient range for the mass spectrum of BBH mergers in an SP (Sections 2.2.1 and 2.2.2), we use the newly upgraded version of BSE code in this work. This code was constructed by Hurley et al. (2000, 2002)

and developed by Banerjee et al. (2020). It is a rapid binary-star evolution code and able to simulate CE evolution, mass transfer, mass accretion, supernova kicks, tidal evolution, mass loss, and angular momentum loss processes.

The latest version of BSE code adds four remnant-mass prescriptions of NS/BH: Belczynski et al. (2008, hereafter B08), Fryer et al. (2012) rapid (hereafter F12-rapid), F12-delayed, and Eldridge & Tout (2004, hereafter ET04) (corresponding to nsflag = 2, 3, 4, and 5 in the code). The B08 remnant mass is obtained from the final CO and FeNi core mass. The F12 remnant mass is obtained by adopting the convection-enhanced neutrino-driven paradigm and has two cases: rapid (explosion happens in the first 250 ms after bounce) and delayed (explosion timescale is greater than 250 ms). The ET04 remnant mass is the final mass before supernova explosions.

The latest version of BSE code also adds the pulsation-pair-instability supernova (PPSN) and pair-instability supernova (PSN) schemes (psflag = 0 and 1 corresponding to inclusion and exclusion in the code). When the temperature is sufficiently high while the density is still rather low, electron-positron pairs would be produced; the internal energy of the pairs will be converted into rest mass, the photon pressure will be reduced, and two cases will occur because of electron-positron pair instability: (i) the outer layers may be ejected for PPSN and (ii) the entire star is disrupted and no remnant is left for PSN (Belczynski et al. 2016a). In this code, if PPSN and PSN are activated (nsflag = 1), PPSN happens when the final mass before supernova explosions m_t is 35–64 M_\odot , and PSN happens when m_t is 64–135 M_\odot .

2.1.2. BPS

In the BPS calculations, we need to generate an initial sample of binaries, which satisfy a certain initial mass function of the primary, and the distributions of the mass ratio ($q = M_2/M_1$, where M_1 and M_2 are the primary and secondary masses, respectively), the orbital period (\bar{P}), and the orbital eccentricity (e). In this work, we use similar distributions to Chruslinska et al. (2018) and Safarzadeh & Farr (2019). These distributions are as follows.

(1) The number distribution of the primary mass is

$$\frac{dN}{dM_1} \propto \begin{cases} M_1^{-1.3} & 0.08 M_\odot \leq M_1 < 0.5 M_\odot, \\ M_1^{-2.2} & 0.5 M_\odot \leq M_1 < 1.0 M_\odot, \\ M_1^{-2.3} & 1.0 M_\odot \leq M_1 < 150 M_\odot. \end{cases} \quad (1)$$

This expression is analogous to the initial mass function of Kroupa et al. (1993).

(2) The mass ratio (q) distribution is a uniform form.

(3) The orbital period distribution can be written as $p(\log_{10}(\bar{P}/\text{days})) \propto (\log_{10}(\bar{P}/\text{days}))^{-0.55}$ in the range [0.15, 5.5].

(4) The orbital eccentricity distribution is expressed as $p(e) \propto e^{-0.42}$ in the range [0.0, 1.0].

According to the above four distributions, we generate 10^7 binary stars in each SP. The SP's metallicity $Z = 0.0001, 0.0003, 0.001, 0.004, 0.01, 0.02,$ and 0.03 .

In the BPS calculations using BSE code, the maximum NS mass is $3 M_\odot$, the dispersion in the Maxwellian distribution for the kick speed $\sigma = 15, 50, 100,$ and 190 km s^{-1} for the standard natal kick mechanism, the maximum lifetime of stars is 13.7 Gyr, and the other model input parameters in the BSE code are the default values. Adopting the above σ is supported by the following facts. By analyzing the observed pulsar sample associated with proper motion, Hansen & Phinney (1997) found that $\sigma = 190 \text{ km s}^{-1}$ is consistent with the observed data. Theoretically, a single star with mass in the range 8–11 M_\odot would end as an ONeMg white dwarf, while Podsiadlowski et al. (2004) found that such a star in a binary system is likely to undergo an electron-capture supernova (ECS). Unlike the slow delayed neutrino-driven explosion, the explosion of an ECS caused by core collapse is prompt, naturally producing an NS with a low-velocity kick. Tauris et al. (2017) found that all known close-orbit BNS systems would experience an ultra-stripped phase (during which the mass is extremely stripped by its close-orbit compact object), the mass of the ultra-stripped star is relatively small, it would undergo accretion-induced collapse (AIC), and it would produce an NS with low-velocity kick. To explain the observation that seven Galactic BNS systems exhibit a remarkably well-defined relation between the pulsar spin period and the orbital eccentricity, Dewi et al. (2005) demonstrated that the second formed NS must receive a small kick with $\sigma < 50 \text{ km s}^{-1}$.

2.2. Basic Components of a Phenomenological Model for the Cosmic GW Merger Events

2.2.1. BBH and BNS Merger Efficiency

For an SP with mass M_{SP} and metallicity Z , we define the BBH merger efficiency, f_{BBH} , as

$$f_{\text{BBH}} = \frac{N_{\text{BBH}}}{M_{\text{SP}}}, \quad (2)$$

where N_{BBH} is the number of BBH mergers for an SP during 13.7 Gyr. Using BSE code, we get the BPS results and the $f_{\text{BBH}}-Z$ relationship for four remnant-mass prescriptions (B08, F12-rapid, F12-delayed, and ET04), two PPSN/PSN patterns (inclusion or exclusion), and four σ values ($\sigma = 15, 50, 100,$ and 190 km s^{-1}). The results are shown in Figure 1. From it, we see that (i) f_{BBH} decreases linearly with $\log_{10}(Z/Z_\odot)$ and the slope hardly varies for most BPS calculations. The reason is that the mass loss caused by stellar wind is proportional to Z . Therefore, in this work we use the following form to

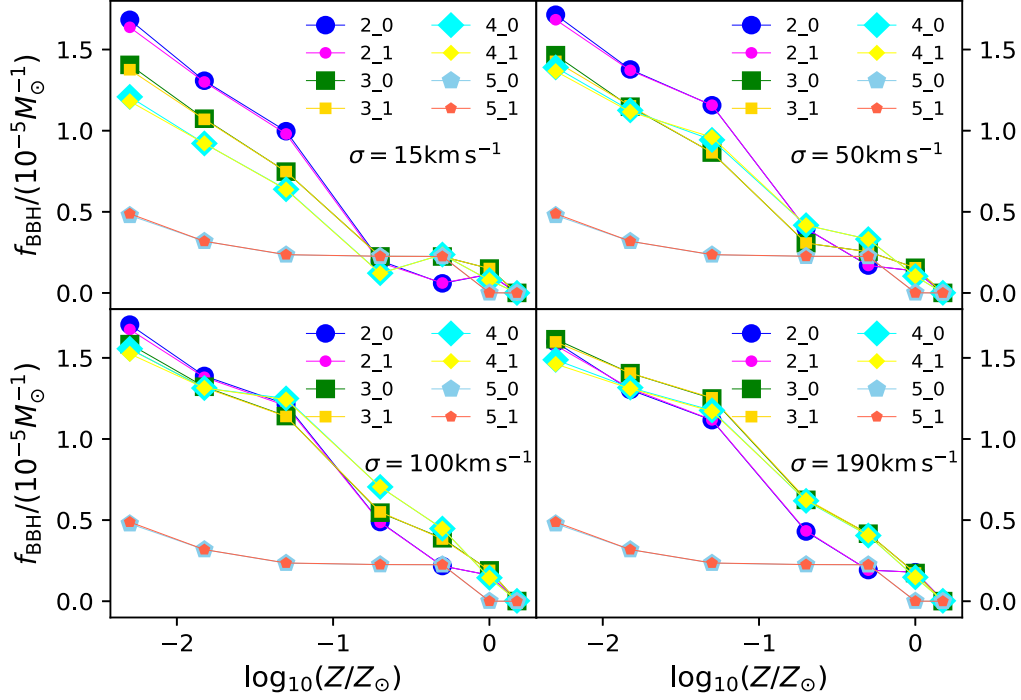


Figure 1. BBH merger efficiency f_{BBH} as a function of metallicity $\log_{10}(Z/Z_{\odot})$ for BPS calculations with different remnant-mass (nsflag) prescriptions, SN (psflag) patterns, and kick velocities. The labels in each panel stand for nsflag_psflag. For example, 2_1 is for nsflag = 2 and psflag = 1. The top left, top right, bottom left, and bottom right panels are for $\sigma = 15, 50, 100,$ and 190 km s^{-1} , respectively.

approximate the $f_{\text{BBH}}\text{-}\log_{10}(Z/Z_{\odot})$ relationship:

$$f_{\text{BBH}} = f_0 + \epsilon \log_{10}(Z/Z_{\odot}) \quad 0.0001 \leq Z \leq 0.03, \quad (3)$$

where f_0 is a constant; ϵ is the slope and it has an important effect on studying the host galaxy of a BBH merger. (ii) The choice of remnant-mass scheme (nsflag) has a larger effect on the $f_{\text{BBH}}\text{-}Z$ relation. The slopes are similar among B08, F12-rapid, and F12-delayed (nsflag = 2, 3, and 4) models, which are greater than that of ET04 (nsflag = 5). (iii) The choices of PPSN/PSN switch (psflag) and σ have small impacts on the $f_{\text{BBH}}\text{-}Z$ relation. Some studies showed that f_{BBH} does not vary with Z at very low metallicities. The mean metallicity of the universe at most of the time is in the range $0.01 Z_{\odot}\text{-}Z_{\odot}$ (close to the mean metallicity today, Dvorkin et al. 2016), so the usage of a linear $f_{\text{BBH}}\text{-}\log_{10}(Z/Z_{\odot})$ relation is reasonable in this work.

Similarly, we define the BNS merger efficiency, f_{BNS} , as

$$f_{\text{BNS}} = \frac{N_{\text{BNS}}}{M_{\text{SP}}}, \quad (4)$$

where N_{BNS} is the number of BNS mergers for an SP during 13.7 Gyr. Our result for the $f_{\text{BNS}}\text{-}Z$ relation is shown in Figure 2. From it, we see that (i) f_{BNS} hardly varies with Z except at $Z = 0.0001$. The proportion of stars with $Z = 0.0001$ in the local universe is small, so we set $f_{\text{BNS}} = \text{const.}$ for a given remnant-mass prescription, PPSN/PSN pattern, and kick

velocity in this work. (ii) f_{BNS} depends strongly on the remnant-mass prescription and σ . The value of f_{BNS} is larger for the F12-delayed model than for the F12-rapid model. The value of f_{BNS} when $\sigma = 50 \text{ km s}^{-1}$ (top right panel) is bigger than that for $\sigma = 190 \text{ km s}^{-1}$ (bottom right panel). (iii) The f_{BNS} value near $Z = 0.1 Z_{\odot}$ is the minimum one for most of the cases in the top panels of Figure 2. This phenomenon is similar to that found by using a low CE ejection efficiency (Giacobbo & Mapelli 2019; Santoliquido et al. 2021, while f_{BNS} is nearly independent of metallicity when using a high CE ejection efficiency). This trend is mainly caused by the stellar radii of progenitors with mass around $8\text{-}20 M_{\odot}$. Their stellar radii are significantly larger at $Z = 0.1 Z_{\odot}$ than at other metallicities.

To test our $f_{\text{BBH}}\text{-}Z$ and $f_{\text{BNS}}\text{-}Z$ relations, we compare them with previous works. First, we compare with the results of Giacobbo & Mapelli (2018), which used an updated version of BSE code (i.e., MOBSE code, Mapelli et al. 2017; Giacobbo et al. 2018), and find that our results are consistent with theirs. Figure 14 in Giacobbo & Mapelli (2018) shows that f_{BNS} is almost independent of metallicity when using a high CE ejection efficiency, its value near $Z = 0.1 Z_{\odot}$ is the minimum when using a low CE ejection efficiency, while f_{BBH} decreases with metallicity. Second, in Figure 3 we compare with those of Chruslinska et al. (2018), which are obtained by using STARTRACK code (Belczynski et al. 2002, B08). In Figure 3, we give seven model results (reference, BE1, C, P,

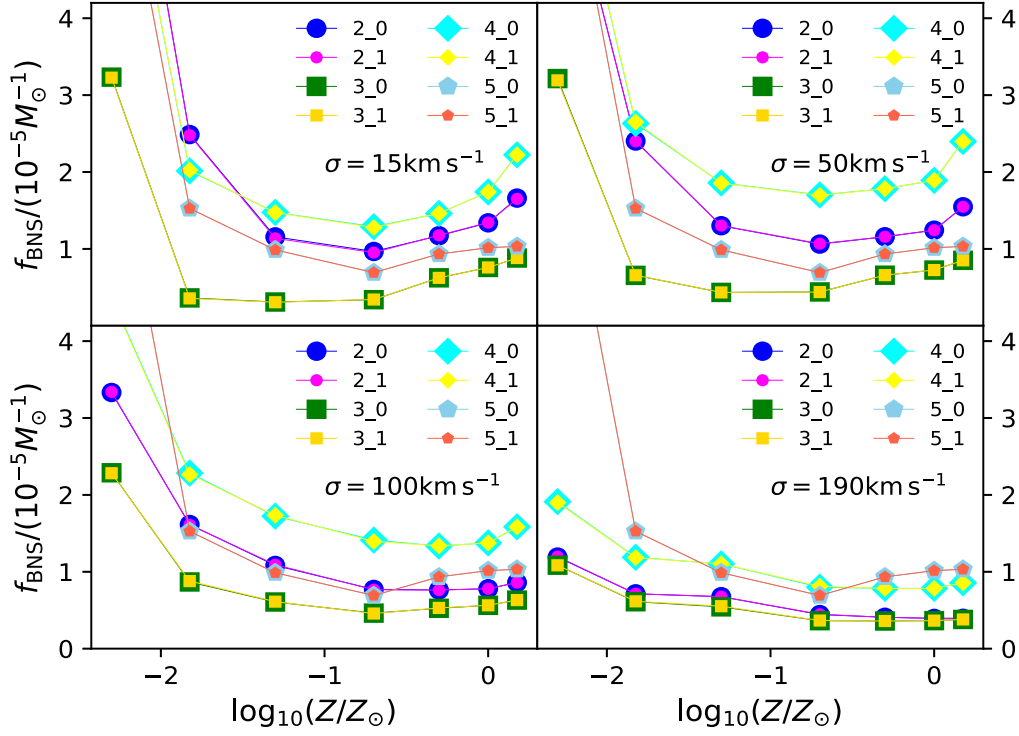


Figure 2. Same as Figure 1, but for BNS merger efficiency f_{BNS} .

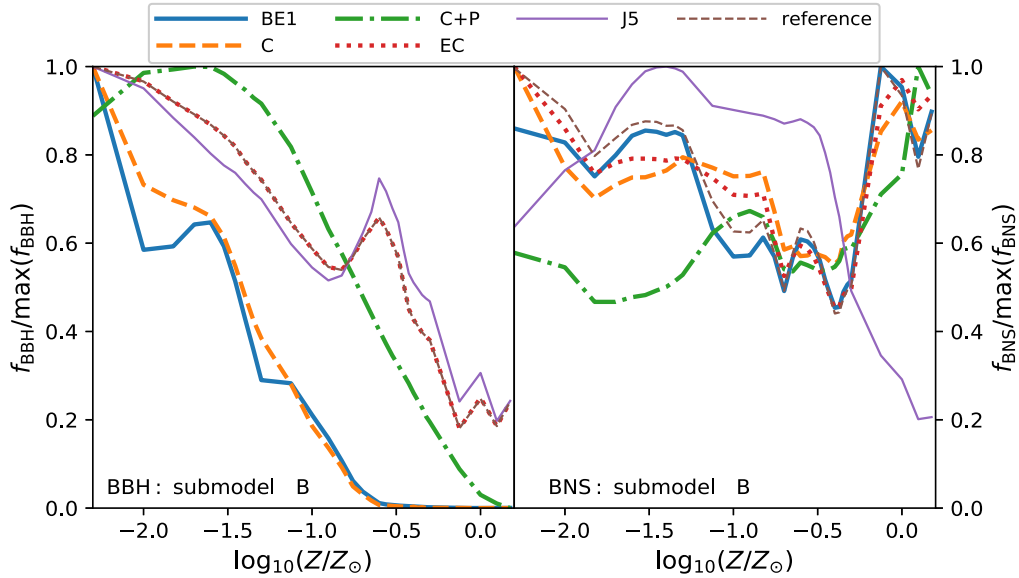


Figure 3. The merger efficiencies f_{BBH} and f_{BNS} of Chruslinska et al. (2018) BBH (left panel) and BNS (right panel) as functions of metallicity $\log_{10}(Z/Z_{\odot})$. For the sake of clarity, we set the maximum values of f_{BBH} and f_{BNS} ($\max(f_{\text{BBH}})$ and $\max(f_{\text{BNS}})$) to 1. An introduction to each model is given in the text.

C+P, EC, and J5) of Chruslinska et al. (2018) in the case of excluding binaries undergoing a CE initiated by Hertzsprung Gap (HG) stars, e.g., submodel B. In the case of submodel B, the model local BBH merger rate agrees with observations,

while in the case of submodel A (including the binaries undergoing CE initiated by HG stars), the model local BH–BH merger rate is larger than observations. The reference model is their standard model. The reference model uses

$\sigma = 265 \text{ km s}^{-1}$ for CCSN (Hobbs et al. 2005) and $\sigma = 0$ for ECS and AIC. In the other models, only a specific factor is varied; the rest are kept the same as in the reference model. The BE1 model uses the natal kick of Bray & Eldridge (2016) for CCSN ($v_{\text{nk}} = 70(M_{\text{ej}}/M_{\text{rem}}) + 120 \text{ km s}^{-1}$). The C model uses the same natal kick for CCSN as the BE1 model and low angular momentum loss. The C+P model uses variations of models C and P. The P model uses a stable thermal mass transfer for an HG+NS/BH binary (CE evolution in the reference model). The EC model uses the lower and upper mass limits of 1.63 and 2.45 for the ECS progenitors (1.26 and 2.25 in the reference model). The J5 model uses the conservative case for the angular momentum loss (half-conservative mass transfer in the reference model). Comparing f_{BBH} of Chruslinska et al. (2018) in the left panel of Figure 3 with ours in Figure 1, we find that all models of $f_{\text{BBH}} - \log_{10}(Z/Z_{\odot})$ linearly decrease with Z . Comparing f_{BNS} of Chruslinska et al. (2018) in the right panel of Figure 3 with ours in Figure 2, we find that all model f_{BNS} are constant for a given remnant-mass prescription, PPSN/PSN pattern, and kick velocity.

After the determinations of the $f_{\text{BBH}}-Z$ and $f_{\text{BNS}}-Z$ functional forms, for convenience, we define $\zeta = \epsilon/f_0$ and $\eta = f_{\text{BNS}}/f_0$. From Figures 1 and 2, we see that ζ is near -6 for nsflag = 2, 3, and 4, and η in the range $[0, 20]$. In the calculations of Section 2.3, ζ and η will be varied in their corresponding regions.

2.2.2. Mass Spectrum of a BBH Merger

We use an analytic form to describe the mass spectrum of a BBH merger, which is from Abbott et al. (2020b). m_1 and m_2 are the primary and secondary BH masses for a BBH merger, respectively. The primary mass distribution for BBH mergers formed in an SP satisfies a power function with an exponent α :

$$p(m_1) \propto m_1^{-\alpha} \quad \gamma < m_1 < m_{\text{max}}, \quad (5)$$

where γ and m_{max} are the minimum and maximum BH masses. Our BPS calculations reveal that the value of γ hardly varies with metallicity, but m_{max} depends strongly on the progenitor's metallicity Z . m_{max} drops rapidly with metallicity—its trend is similar to a power-law function. Therefore, we assume that γ is a constant at all metallicities, and m_{max} satisfies the following form:

$$m_{\text{max}} = \frac{m_0}{(1-a)(Z/Z_{\odot})^b + a}, \quad (6)$$

where m_0 , a , and b are the free parameters. When $a=0$, this formula is a power function. Figure 4 shows a comparison between this equation ($m_0 = 14.746 M_{\odot}$, $a = 0.1514$, and $b = 0.682$) and the results of Belczynski et al. (2010), which is a representative work before a GW signal had been directly detected. To obtain the ranges of the free parameters m_0 , a , and b , we first carry out lots of BPS calculations, in which the initial mass $M_1 = 150$ or $300 M_{\odot}$ and orbital period $\bar{P} = 10^8$ days

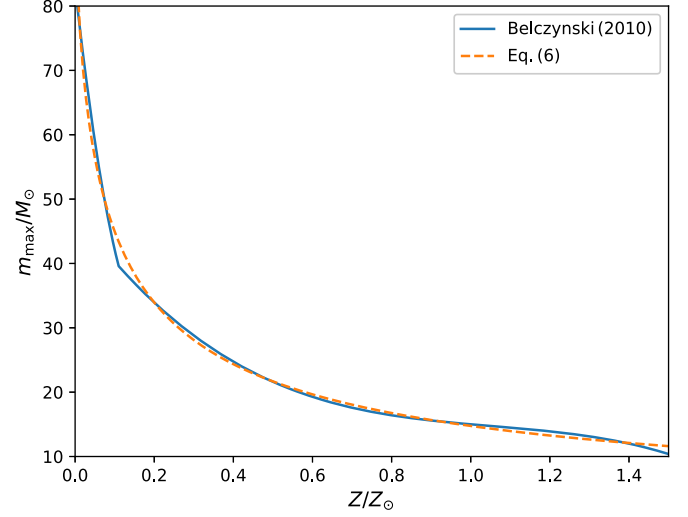


Figure 4. The maximum BH mass m_{max} as a function of metallicity Z/Z_{\odot} . The solid line is for Belczynski et al. (2010). The dashed line is for Equation (6) with $m_0 = 14.746 M_{\odot}$, $a = 0.1514$, and $b = 0.682$.

(mimicking a single star), to obtain the $m_{\text{max}} - Z$ relations, then use Equation (6) to fit the above $m_{\text{max}} - Z$ relation. The $m_{\text{max}} - Z$ relations given by BPS calculations and Equation (6) are shown in Figure 5. Through fitting these results, we get the ranges of m_0 , a , and b . The parameter a is in the range $[0.03, 0.23]$ and b is in the range $[0.37, 1.2]$ when m_0 is near $10 M_{\odot}$ or $15 M_{\odot}$. In this work, we set m_0 to $15 M_{\odot}$.

We also assume the mass-ratio distribution for two components in a BBH merger satisfies a power function, in combination with Equation (5), then the mass distribution of BBH mergers in an SP is

$$\begin{aligned}
 p(m_1, m_2 | \lambda, Z) &\propto p(m_1) \left(\frac{m_2}{m_1} \right)^{\beta} \Theta(m_2 \leq m_1) \\
 &\propto m_1^{-\alpha} \left(\frac{m_2}{m_1} \right)^{\beta} \Theta(m_2 \leq m_1), \quad (7)
 \end{aligned}$$

where β is the exponent of the power function for the mass ratio of two components in a BBH merger, λ represents the set of free parameters $\{\alpha, \gamma, a, b, \beta\}$, and Θ is the Heaviside step function.

2.2.3. Delay Time

Due to the GW emission, the orbital separations of compact binaries will decrease. The delay time is defined as the time between the birth of the compact binary system and its final merger. The evolution lifetime is determined by both the stellar nuclear lifetime and the delay time caused by the GW emission. In the phenomenological model, we assume that the delay time is weakly correlated with the component masses in a compact binary. The probability distribution of the delay time τ is

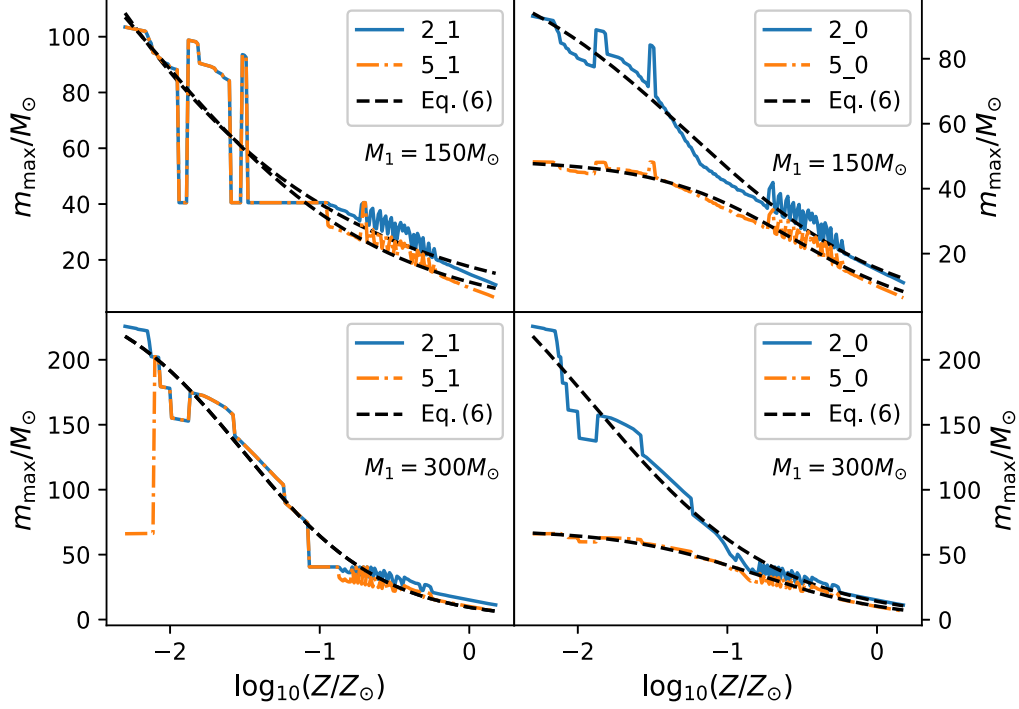


Figure 5. The maximum BH mass m_{\max} as a function of metallicity $\log_{10}(Z/Z_{\odot})$ for our BPS calculations (solid lines and dotted–dashed lines) and Equation (6) with different parameters (dashed lines). The top and bottom panels are for the initial mass $M_1 = 150 M_{\odot}$ and $300 M_{\odot}$. The labels in each panel stand for `nsflag_psflag`.

approximately expressed as (Simonetti et al. 2019; Molero et al. 2021)

$$p(\tau) = \begin{cases} 0 & \tau < 10 \text{ Myr}, \\ p_1 & 10 \text{ Myr} \leq \tau \leq 40 \text{ Myr}, \\ p_2 \tau^{-1} & 40 \text{ Myr} < \tau < 13.7 \text{ Gyr}, \end{cases} \quad (8)$$

where p_1 and p_2 are constants.

2.2.4. Cosmological Model and the Evolutions of SFR and Metallicity with Redshift

A flat cosmology with the cosmological parameters $(\Omega_M, \Omega_{\Lambda}, \Omega_k, h) = (0.308, 0.692, 0.0, 0.6781)$ (Planck Collaboration et al. 2016) is used in this work. In a flat cosmology, the look-back time t at redshift z is

$$t(z) = \frac{1}{H_0} \int_0^z \frac{dz'}{(1+z')E(z')}, \quad (9)$$

where the Hubble constant $H_0 = 100h \text{ km s}^{-1} \text{ Mpc}^{-1}$ and $E(z') = \sqrt{\Omega_M(1+z')^3 + \Omega_{\Lambda}}$. The comoving distance (D_c) can be expressed as

$$D_c(z) = \frac{c}{H_0} \int_0^z \frac{dz'}{E(z')}, \quad (10)$$

where c is the speed of light in vacuum, and H_0 and $E(z')$ have the same meanings as Equation (9). Via the comoving distance

D_c , the luminosity distance (D_L) can be easily computed from

$$D_L = (1+z)D_c. \quad (11)$$

The redshift derivative of the comoving volume (V_c), in combination with Equation (11), is expressed as

$$\frac{dV_c}{dz} = \frac{4\pi c}{H_0} \frac{D_L^2}{(1+z)^2 E(z)} = \frac{4\pi c}{H_0} \frac{(1+z)^2 D_c^2}{(1+z)^2 E(z)} = \frac{4\pi c}{H_0} \frac{D_c^2}{E(z)} \quad (12)$$

For convenience, we define $A(z_{\max})$ as

$$A(z_{\max}) = \int_0^{z_{\max}} \frac{1}{1+z} \frac{dV_c}{dz} dz, \quad (13)$$

and set $z_{\max} = 1$, beyond which no GW sources can be detected for GWTC-1 (Abbott et al. 2020b).

The calculations of cosmic BBH/BNS GW mergers need the evolutions of cosmic SFR density ($\psi(z)$) and the mean metallicity ($Z_{\text{mean}}(z)$) with redshift. In this work, we use the evolution of cosmic SFR density with redshift of Madau & Dickinson (2014), which has also been used in the work Chruslinska et al. (2018) and Belczynski et al. (2016b),

$$\psi(z) = 0.015 \frac{(1+z)^{2.7}}{1 + [(1+z)/2.9]^{5.6}} M_{\odot} \text{ Mpc}^{-3} \text{ yr}^{-1}. \quad (14)$$

Moreover, we use the evolution of mean metallicity with redshift of Belczynski et al. (2016b) and Vangioni et al. (2015),

$$Z_{\text{mean}}(z) \propto \frac{y(1-R)}{\rho_b} \int_z^{z_0} \frac{97.8 \times 10^{10} \psi(z')}{H_0 E(z')} dz', \quad (15)$$

where the metal yield $y = 0.019$, the return fraction $R = 0.27$, ρ_b is baryon density, and $\psi(z')$, H_0 , and $E(z')$ have the same meanings as in Equations (14) and (9). In this work, we assume that Z_{mean} at redshift $z = 0$ is equal to Z_0 (in units of Z_\odot), which varies in the range [0.1, 1.0].

2.3. The Determinations of the Model Free Parameters and Result

We use the Bayesian method, in combination with the key ingredients of the phenomenological model for the cosmic GW merger events and the posterior mass and redshift sample for the observed GWTC-1 BBH event, to present the posterior and results for the free parameters.

2.3.1. The Posterior Probability Distribution of Free Parameter via the Bayesian Method

First, the differential mass–redshift–metallicity distribution of BBH mergers is defined as

$$\frac{dN_{\text{merger}}}{dm_1 dm_2 dz dZ} = \mathcal{N} p(m_1, m_2, z, Z), \quad (16)$$

where \mathcal{N} is the total number of BBH mergers across all masses, redshifts, and metallicities. The integral of the probability of the mass–redshift–metallicity distribution $p(m_1, m_2, z, Z)$ is 1. We assume that the mass distribution does not vary across cosmic time, so $p(m_1, m_2, z, Z)$ can be decomposed into two parts,

$$p(m_1, m_2, z, Z) = p(m_1, m_2 | \lambda, Z) p(z, Z), \quad (17)$$

where $p(m_1, m_2 | \lambda, Z)$ is given by Equation (7).

If the i th BBH merger event happens at redshift z , and its progenitor is born in an SP with metallicity Z and redshift z' , in combination with Equation (17), the probability of this merger event is

$$p_i(m_1, m_2, z, Z) \propto p(m_1, m_2 | \lambda, Z) \frac{1}{1+z} \frac{dV_c}{dz} \psi(z', Z) f_{\text{BBH}}(Z), \quad (18)$$

where the factor of $1/(1+z)$ is used to convert from the rest frame to the observer frame, dV_c/dz is the redshift derivative of the comoving volume (Equation (12)), $\psi(z', Z)$ is the fractional SFR at redshift z' for metallicity Z , and $f_{\text{BBH}}(Z)$ is the BBH merger efficiency (Equation (2)). The redshift z' and metallicity Z of the progenitor are unknown, but we can use the delay time distribution $p(\tau)$ (Equation (8)) to estimate them. On average, from Equation (18), the probability of the i th merger event can

be rewritten as

$$p_i(m_1, m_2, z) \propto \frac{1}{1+z} \frac{dV_c}{dz} \int_z^{z_0} \int_z^\infty p(m_1, m_2 | \lambda, Z) \times \psi(z', Z) f_{\text{BBH}}(Z) p(\tau) dz' dZ, \quad (19)$$

where $\tau = t(z') - t(z)$ and $p(\tau)$ is the delay time distribution (Equation (8)). For simplify our work, we assume $\psi(z', Z)$ can be replaced by $\psi(z') \delta(Z - Z_{\text{mean}})$, where δ stands for the delta function, and ψ and Z_{mean} are described by Equations (14) and (15), respectively. Finally, the above probability can be rewritten as

$$p_i(m_1, m_2, z) \propto \frac{1}{1+z} \frac{dV_c}{dz} \int_z^\infty p(m_1, m_2 | \lambda, Z_{\text{mean}}) \times \psi(z') f_{\text{BBH}}(Z_{\text{mean}}) p(\tau) dz', \quad (20)$$

Not all GW signals can be detected by the detector. Only those with high signal-to-noise ratio (S/N) can be identified. So the probability of observing the i th merge event is (Safarzadeh & Farr 2019)

$$p_{\text{obs}}(m_1, m_2, z) = p_i(m_1, m_2, z) P(\text{det} | m_1, m_2, z), \quad (21)$$

where $P(\text{det} | m_1, m_2, z)$ is the probability of detection for a GW detector and it relates only to the GW signal's S/N. $P(\text{det} | m_1, m_2, z)$ is in the range 0–1. We assume that sources would be detected if they have $S/N > 8$ (Fishbach et al. 2018). S/N can be calculated from

$$(S/N)^2 = 4 \int \frac{|h(\nu)|^2}{S_n(\nu)} d\nu, \quad (22)$$

where ν is the frequency, $h(\nu)$ is the GW strain, and $S_n(\nu)$ is the noise power spectral density of the GW detectors. For the merger events in GWTC-1, we calculated their S/N by using the IMRPhenomPv2 waveform model (Hannam et al. 2014; Husa et al. 2016; Khan et al. 2016) and the Advanced LIGO Early High Sensitivity noise power spectral density (Abbott et al. 2018). In the calculations of S/N, we set the spin of all compact binary stars to zero and assume that the sources are isotropically distributed on the sky and that the binary inclination is uniformly distributed on the sphere (Fishbach et al. 2018). Under these assumptions, $P(\text{det} | m_1, m_2, z)$ is predominantly determined by the component masses and the redshift.

Our model of the BBH merger event has seven parameters. The symbol Λ represents the total set of free parameters $\{\alpha, a, b, \gamma, \beta, \zeta, Z_0\}$ (Z_0 is the mean metallicity at redshift $z = 0$, see the text below Equation (15)). Λ contains $\lambda \{\alpha, a, b, \gamma, \beta\}$. Our Bayesian analysis method is the same as that used in Fishbach et al. (2018), Abbott et al. (2020b), and Safarzadeh & Farr (2019). If the number of observed BBH merger events is N_{obs} ($N_{\text{obs}} = 10$ in GWTC-1), in combinations with Equations (20) and (21), a posterior of the hyperparameter (Λ) given by the set of observed data $\{D_i\}$ (Fishbach et al. 2018;

Abbott et al. 2020b) is

$$p(\Lambda|\{D_i\}) \propto \pi(\Lambda) \prod_{i=1}^{N_{\text{obs}}} \frac{L(\{D_i\}|\Lambda)}{\rho(\Lambda)}, \quad (23)$$

where $\pi(\Lambda)$ is a prior, $L(\{D_i\}|\Lambda)$ is the marginal likelihood for the i th GW merger event,

$$\begin{aligned} L(\{D_i\}|\Lambda) &\propto \frac{1}{A(z_{\text{max}})} \int dm_1 dm_2 dz dz' [p(m_1, m_2|\Lambda, Z_{\text{mean}}) \\ &\times \frac{1}{1+z} \frac{dV_c}{dz} f_{\text{BBH}}(Z_{\text{mean}}) \psi(z') p(\tau) p(\{D_i\}|m_1, m_2, z)], \end{aligned} \quad (24)$$

and

$$\begin{aligned} \rho(\Lambda) &\propto \frac{1}{A(z_{\text{max}})} \int dm_1 dm_2 dz dz' [p(m_1, m_2|\Lambda, Z_{\text{mean}}) \\ &\times \frac{1}{1+z} \frac{dV_c}{dz} f_{\text{BBH}}(Z_{\text{mean}}) \psi(z') p(\tau) P(\det|m_1, m_2, z)], \end{aligned} \quad (25)$$

where $A(z_{\text{max}})$ is given by Equation (13). The probability $p(\{D_i\}|m_1, m_2, z)$ in Equation (24) can be obtained from the posterior sample for the observed individual GWTC-1 event (Abbott et al. 2019b).⁵ We calculate the posterior probability density of model parameters by using Python MultiNest module (Feroz et al. 2009; Buchner et al. 2014).

2.3.2. Results of Free Parameters

Figure 6 shows the posterior distribution for seven parameters in the set of Λ . (i) From the first column, we see that the mean value of α (the exponent of the primary mass distribution for BBH mergers formed in an SP, see Equation (5)) is 1.65 and close to the result of Fishbach et al. (2018). (ii) The maximum BH mass m_{max} at $Z=0$ is $15 M_{\odot}/a$ (see Equation (6)). From the second column, we see that $a=0.16$, so the mean $m_{\text{max}} = 93^{+73}_{-22} M_{\odot}$ in our model. This value is close to the maximum BH mass found by GWTC-3 (Abbott et al. 2021). (iii) Because the peak in the observed m_1 distribution is close to $32 M_{\odot}$, the minimum BH mass γ (see Equation (5)) in the fourth column tends to become big, and its mean value is $\gamma = 7.9^{+1.45}_{-3.03} M_{\odot}$. (iv) From the fifth column, we see the mean value of β (the exponent of the power function of the mass-ratio distribution for BBH mergers, see Equation (7)) is 13.53. This means the mass ratio of BBH mergers tends to 1. (v) The distribution of ζ ($= \epsilon/f_0$, the slope of the $f_{\text{BBH}} - \log_{10}(Z/Z_{\odot})$ relation, see Equation (3)) which is close to a uniform distribution in the sixth column of Figure 6; its mean value is -8.32 , but four of five panels associated with ζ (the sixth low of Figure 6) show its probability reaches a maximum near $\zeta = -12$. (vi) From the last column, we see that the mean

metallicity at $z=0$, Z_0 , has two optimal values: one is around $0.2 Z_{\odot}$ and the other is near $0.9 Z_{\odot}$. Three peaks exist in the ζ - Z_0 panel.

3. Host Galaxy of a Merger Event

3.1. Empirical Galaxy Model

There exist several pathways to get the evolutionary patterns of galaxies, such as semianalytic models and empirical models. A minimum number of free parameters are included in the empirical models, which makes the fitting procedure to the observed data more accurate and rapid. We use the mock galaxy catalog generated by the EMERGE empirical galaxy code (Moster et al. 2018)⁶ to study the probability of a merger event. The EMERGE catalog includes the galaxy properties (such as stellar mass) at 94 redshifts. In this work, we only use the data on stellar mass and SFR of each mock galaxy.

The EMERGE model can describe the evolution of an individual galaxy in a volume since $z \sim 10$ with the aid of the GADGET cosmological N -body simulation code (Springel 2005), which simulates the formation and evolution of dark matter. Adopting the classical χ^2 methodology and Markov Chain Monte Carlo (MCMC) method, the EMERGE model can well reproduce the observed data spanning from the local universe to high redshifts, such as cosmic SFR densities, sSFR, stellar mass functions, and quenched fractions. The observed data about the fraction of quenched galaxies as a function of the galaxy's stellar mass are used, so the empirical EMERGE galaxy model can perfectly predict the red galaxies lacking young blue stars. Moreover, the empirical EMERGE galaxy model is a good tool for studying the host galaxy of mergers of double compact stars. NGC 4993, the host galaxy of BNS merger GW170817, is a quenched galaxy, and this is also one of the reasons we use the EMERGE catalog.

3.2. Calculating a Galaxy's Metallicity, Age, and Normalized Probability

3.2.1. Calculating a Galaxy's Metallicity

The empirical model does not include models of evolutionary population synthesis and galaxy chemical evolution, so it is unable to provide the metallicity of a galaxy. Here, we derive the metallicity of a galaxy ($12 + \log_{10}[\text{O}/\text{H}]$) by adopting the fitting formula of Chruslinska & Nelemans (2019) for the observed mass-metallicity relation:

$$12 + \log_{10}[\text{O}/\text{H}] = Z_{\text{O}/\text{H asy m}} - \log_{10} \left[1 + \left(\frac{M_*}{M_{\text{TO}}} \right)^{-\delta} \right], \quad (26)$$

⁵ <https://dcc.ligo.org/LIGO-P1800370/public>

⁶ <https://github.com/bmoster/emerge>

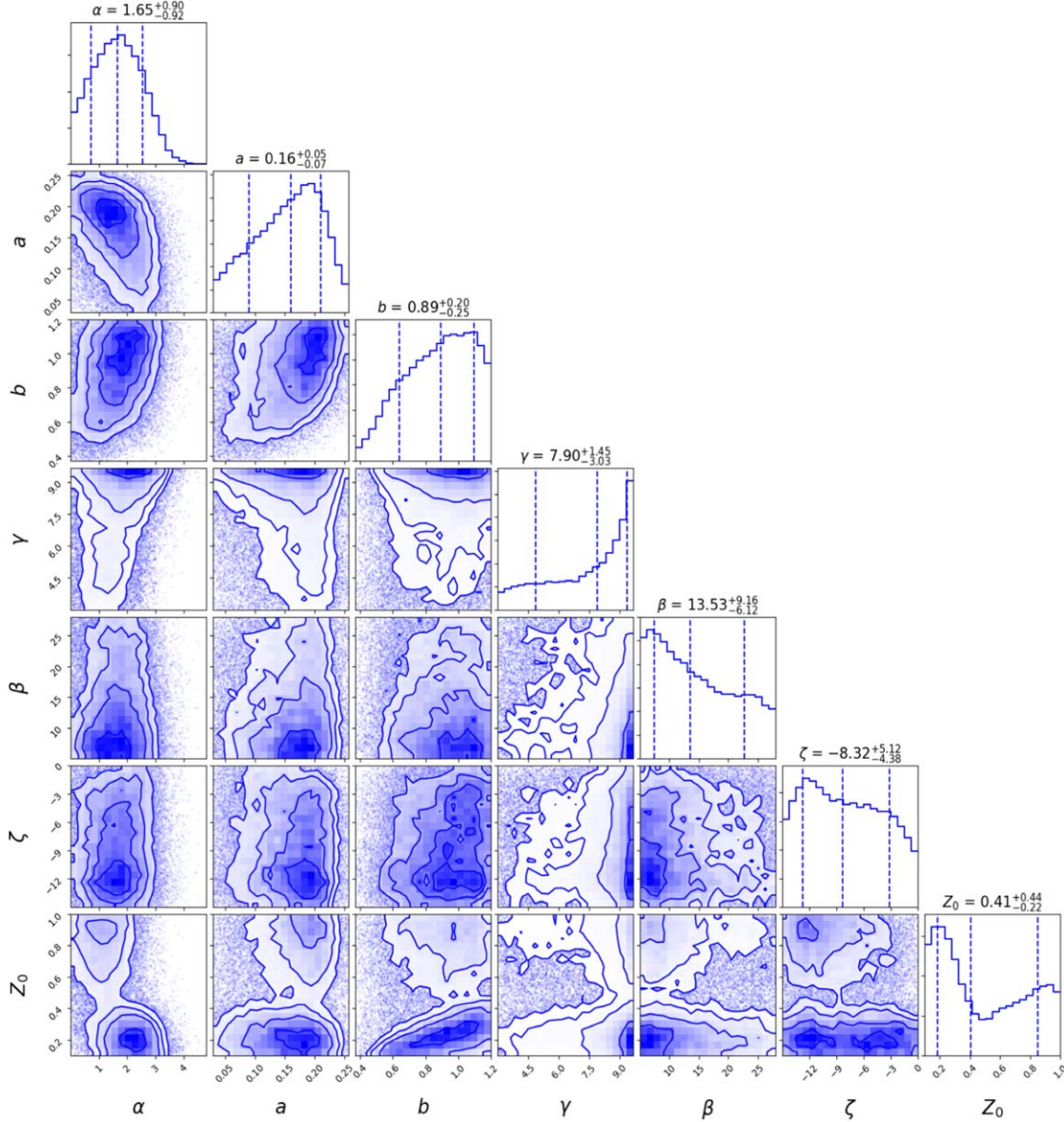


Figure 6. The posterior distributions for seven parameters by fitting 10 BBH merger events in LIGO-O1 and O2 observing runs.

where M_* is the galaxy's stellar mass and M_{TO} is the mass at which the relation begins to flatten. The parameters δ and M_{TO} at redshifts $z=0.0, 0.7, 2.2,$ and 3.5 are taken from Table 2 (i.e., their T04 model) of Chruslinska & Nelemans (2019). Using $12 + \log_{10}[\text{O}/\text{H}] = 8.66$ for solar metallicity, we can translate $12 + \log_{10}[\text{O}/\text{H}]$ to $\log_{10}Z$ and Z . Using the posterior distribution of Z_0 (mean metallicity at $z=0$, see Equation (15)) in Figure 6, Equation (15), and the SFR-weighted metallicity derived from Equation (26), we can obtain $Z_{\text{O/H asy}}$ at different redshifts. In order to generate a distribution in the metallicity–mass panel (the top panels of Figure 7), in this work we set the dispersion of this relation to 0.3 dex, which is also used in the work of Mapelli et al. (2018).

3.2.2. Calculating a Galaxy's Age

The EMERGE code creates 94 snapshots from redshift $z \sim 10$ to $z=0.0$, and the scale factor \bar{a} (i.e., $\bar{a} = 1/(1+z)$) is equally spaced ($\Delta\bar{a} = 0.01$). We calculate the age of a galaxy from the following equation:

$$\text{age}_i = \frac{\sum_j T_j (\Delta M_{*,i,j})}{\sum_j (\Delta M_{*,i,j})}, \quad (27)$$

where T_j is the look-back time of the j th snapshot at redshift z_j , and $(\Delta M_{*,i,j})$ is the newly born stellar mass of the i th galaxy at z_j .

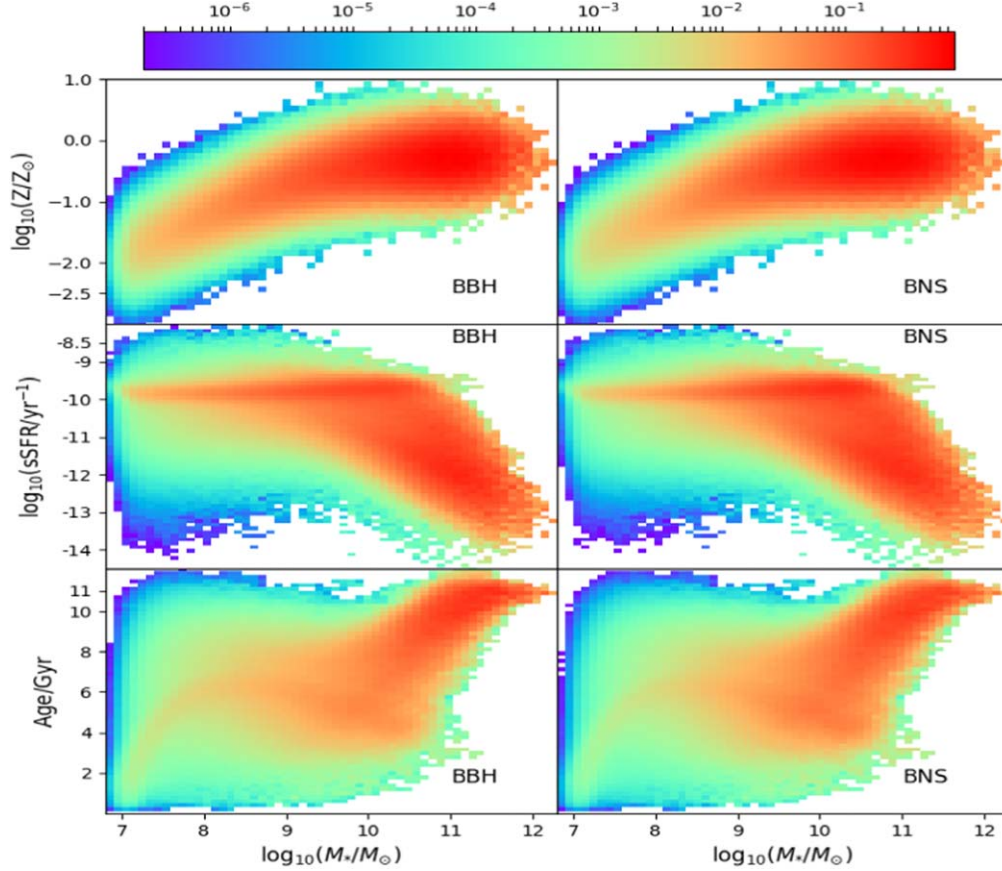


Figure 7. The normalized probability of occurrence of a merger event P in the $\log_{10}(M_*/M_\odot)$ - $\log_{10}(Z/Z_\odot)$, $\log_{10}(M_*/M_\odot)$ - $\log_{10}(\text{sSFR}/\text{yr}^{-1})$, and $\log_{10}(M_*/M_\odot)$ - (age/Gyr) planes for the galaxies with redshift $z \leq 0.1$.

3.2.3. Calculating the Normalized Probability

The probability of occurrence of a merger event, $P(\bar{t})$, is proportional to the number of BBH/BNS mergers that happen in the galaxies. It is entirely unrelated to the GW detector and its corresponding probability of detection. At a given time \bar{t} , it can be calculated from the following equation:

$$P(\bar{t}) \propto \sum_i \int_Z \int_0^{\bar{t}} \psi_i(Z, \bar{t} - \tau) p(\tau) f_{\text{BBH/BNS}}(Z) d\tau dZ, \quad (28)$$

where i stands for the i th galaxy in a bin, in which all galaxies have the same stellar mass, sSFR, age, and metallicity, ψ_i is the SFR of the i th galaxy, $p(\tau)$ is the delay time distribution, and $f_{\text{BBH}}(Z)$ and $f_{\text{BNS}}(Z)$ are the BBH and BNS merger efficiencies, which can be obtained by using the ζ distribution of Figure 6 and $\eta = \text{const}$. Because the values of f_0 and η (see Equation (3)) are not given, we just compute the normalized probability.

3.3. Properties of Host Galaxy

Using the above empirical galaxy model and the posterior distribution of ζ , we can obtain the normalized probability of occurrence of a BBH/BNS merger event, P , for the galaxies with $z \leq 0.1$. In Figures 7 and 8, we show the normalized probability of a merger event as a function of M_* , Z , sSFR, and age.

3.3.1. Stellar Mass

The upper panels of Figure 7 plot the normalized probability of a merger event, P , as functions of M_* and Z for the galaxies with $z \leq 0.1$. We use Equation (26) to calculate Z so that metallicity provides the same information as the stellar mass.

It can be seen from the left panel of Figure 8 that the BBH mergers mostly happen in galaxies with $M_* = 10^{11.1} M_\odot$, and the BNS mergers are most likely detected in galaxies with $M_* = 10^{10.8} M_\odot$, which is similar to the result of Jiang et al. (2020) and close to the stellar mass of NGC 4993 ($4.46 \times 10^{10} M_\odot$, Blanchard et al. 2017). From Section 2.2.1,

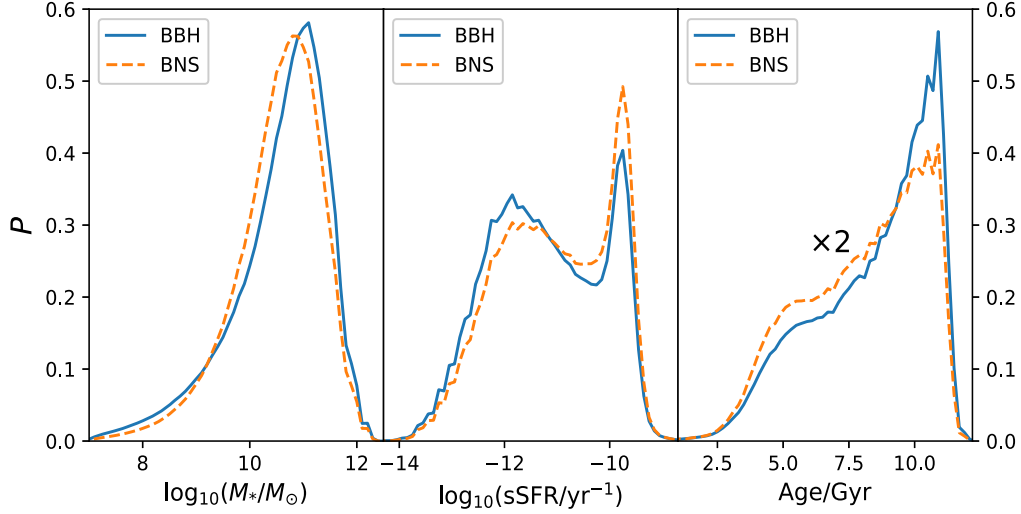


Figure 8. The normalized probability of a merger event P as a function of $\log_{10}(M_*/M_\odot)$ (left), $\log_{10}(\text{sSFR}/\text{yr}^{-1})$ (middle), and age/Gyr (right) for the galaxies with redshift $z \leq 0.1$. The solid line stands for BBH merger. The dashed line represents BNS merger.

we know that ζ depends on Z and η is independent of Z . Figure 8 shows that the probability profile of a BBH merger is similar to that for a BNS merger, so the SP's metallicity does not influence significantly the probability of a merger event.

3.3.2. sSFR

The middle panels of both Figures 7 and 8 show that two kinds of galaxies make a larger contribution to the normalized probability P . One is the quenched galaxies with $\text{sSFR} < 10^{-11} \text{yr}^{-1}$. The results of Jiang et al. (2020), Chu et al. (2022), and Artale et al. (2020) showed that only galaxies with $\text{sSFR} \sim 10^{-10} \text{yr}^{-1}$ have a larger contribution; P decreases rapidly when $\text{sSFR} < 10^{-10} \text{yr}^{-1}$, and $P < 0.05$ at $\text{sSFR} = 10^{-12} \text{yr}^{-1}$. Comparing with their results, the contribution of galaxies with $\text{sSFR} < 10^{-11} \text{yr}^{-1}$ in this work (0.3 at $\text{sSFR} = 10^{-12} \text{yr}^{-1}$) is significantly larger. The reason is that the quenched galaxies make a large contribution to the total SFR at high redshift in the EMERGE empirical galaxy model. Figure 9 plots the contribution to the cosmic SFR density for all the galaxies with $\log_{10}(\text{sSFR}/\text{yr}^{-1}) < -11.0$ in the EMERGE mock galaxy catalog. From it, we can see that the contribution of the quenched galaxies can reach 77% at $z \approx 2.7$, where the corresponding cosmic SFR reaches the maximum value.

From the middle panel of Figure 8, we see that the sSFR value corresponding to the left peak, caused by the quenched galaxies, is near $\log_{10}(\text{sSFR}/\text{yr}^{-1}) = -12$. Blanchard et al. (2017) obtained the result $\log_{10}(\text{sSFR}/\text{yr}^{-1}) = -12.65^{+0.44}_{-0.66}$ for NGC 4993. This value is smaller than ours. The possible reason is as follows. In the comparisons of the EMERGE galaxy model with observations (see Section 3.1), they used the mean sSFR of galaxies, so the sSFR used in this work also is the mean value. If the observed sSFR distribution in the local universe has a tail at the low sSFR end (Salim et al. 2007; Wetzel et al. 2012) or is wider/flatter at

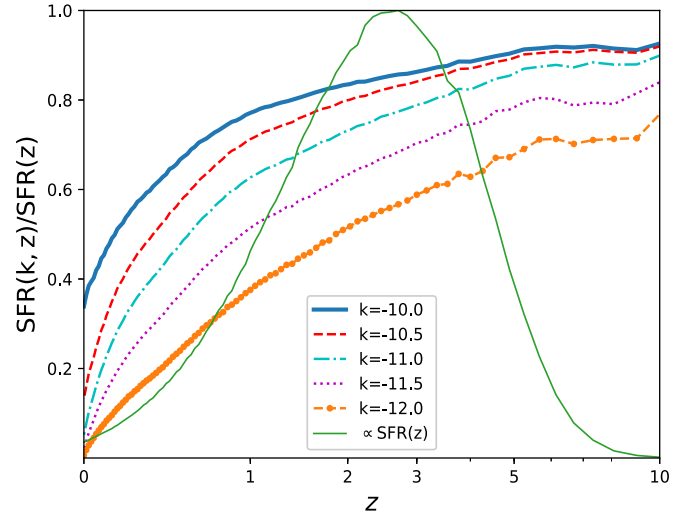


Figure 9. The ratio of the sum of SFR for today's galaxies with $\log_{10}(\text{sSFR}/\text{yr}^{-1}) < k$ to the cosmic SFR density, $\text{SFR}(k, z)/\text{SFR}(z)$, as a function of redshift z . The thick solid line, dashed line, dotted-dashed line, dotted line, and thick circles represent $k = -10.0, -10.5, -11.0, -11.5$ and -12.0 , respectively. The thin solid line is proportional to the cosmic SFR density of Moster et al. (2018).

the low sSFR end (less than 10^{-12}yr^{-1}), the contribution at $\log_{10}(\text{sSFR}/\text{yr}^{-1}) = -12.65$ would increase.

3.3.3. Age

The lower panels of Figure 7 and the right panel of Figure 8 show the normalized probability P of a merger event as a function of the age for their host galaxies, and the results reveal that old

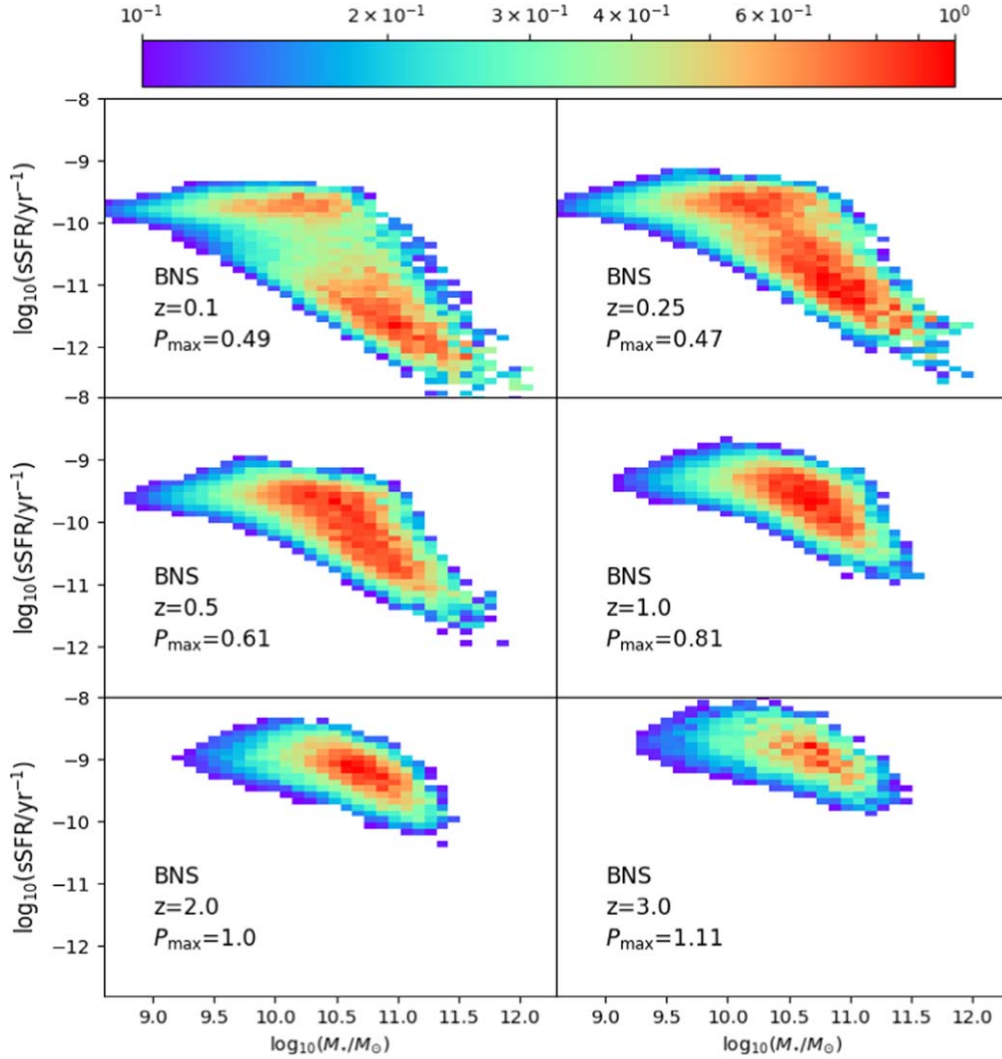


Figure 10. The normalized probability of a BNS merger event P/P_{\max} in the $\log_{10}(M_*/M_{\odot})$ – $\log_{10}(\text{sSFR}/\text{yr}^{-1})$ plane for galaxies at different redshifts (i.e., $z = 0.1, 0.25, 0.5, 1.0, 2.0,$ and 3.0).

galaxies make a larger contribution to P . Note that the P value in the right panel of Figure 8 has been multiplied by 2.

Moreover, it can be seen from the right panel of Figure 8 that the peak is at 11.0 Gyr corresponding to $z \approx 2.7$. In the empirical galaxy model, the peak of cosmic SFR also exists at $z \approx 2.7$ (see Figure 9). Therefore, the peak in the right panel of Figure 8 is mainly caused by the cosmic SFR. The peak is at an age of 6–8 Gyr in the previous studies. The median mass-weighted age of NGC 4993 is $13.2^{+0.5}_{-0.9}$ Gyr (Blanchard et al. 2017). The age of NGC 4993 is slightly greater than the age in our model. This difference may be caused by the following facts.

- (i) The initial orbital period in this work is relatively small. Figures 2 and 4 in Mapelli et al. (2018) show that the delay time distribution has a significant influence on the age. If the delay time distribution is $p(\tau) \sim \tau^{-\kappa}$ with

$\kappa < 1$, $p(\tau)$ become larger at larger τ , the ages of galaxies hosted by BBH and BNS mergers would increase, and the model age corresponding to the peak would agree with that of NGC 4993. Safarzadeh & Farr (2019) have also concluded that $\kappa < 1$. The value of $\kappa < 1$ can be realized by increasing the initial orbital period. If the initial orbital period increases, the delay time of BBH and BNS mergers would increase, $p(\tau)$ at larger τ increases, and κ decreases. Therefore, the smaller initial orbital period in this work may cause the difference in age between the model and NGC 4993.

- (ii) The number of galaxies with age greater than 12 Gyr in the EMERGE catalog is small. The maximum redshift $z = 10$ in the EMERGE model corresponds to the look-back time 13.32 Gyr, but the number of the mock

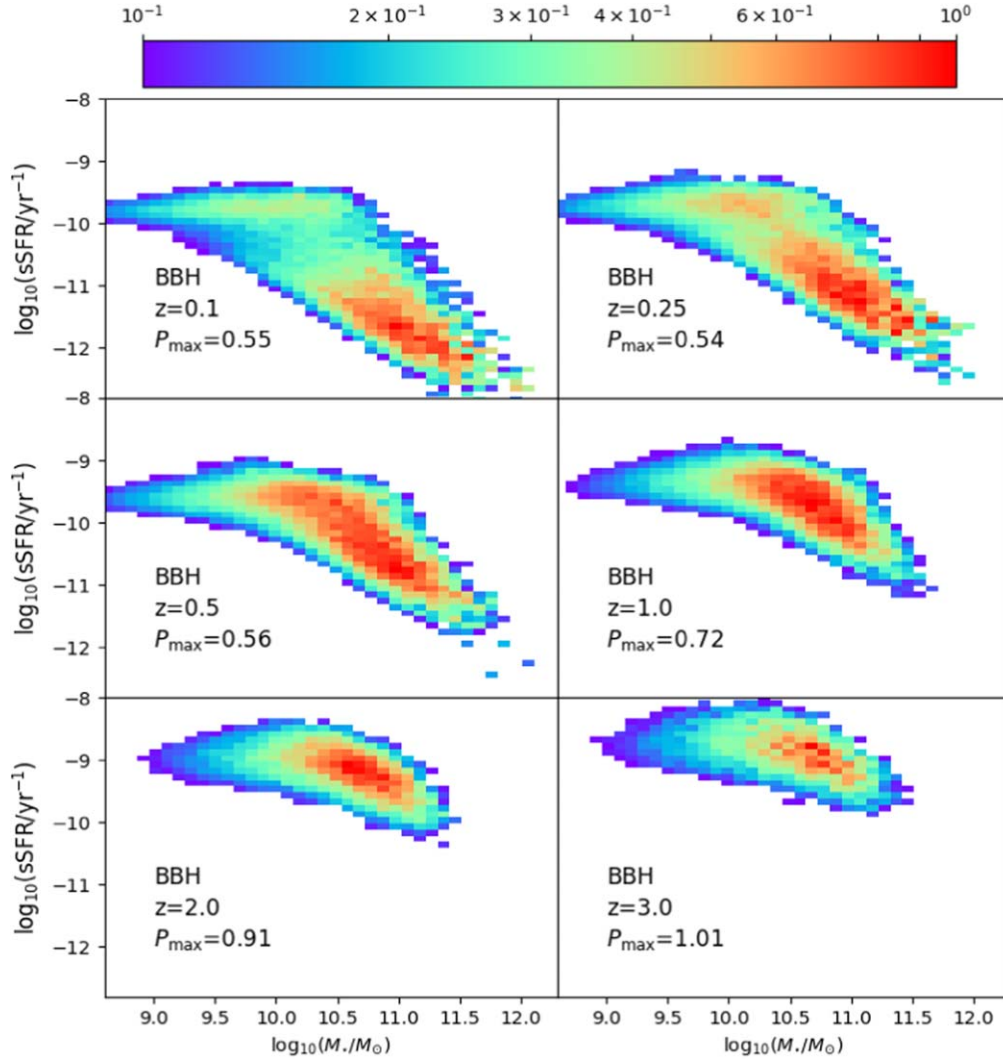


Figure 11. The normalized probability of a BBH merger event P/P_{\max} in the $\log_{10}(M_*/M_{\odot})$ – $\log_{10}(\text{sSFR}/\text{yr}^{-1})$ plane for galaxies at different redshifts (i.e., $z = 0.1, 0.25, 0.5, 1.0, 2.0,$ and 3.0).

galaxies in the EMERGE catalog at $z \approx 10$ is very small. The ages of all mock galaxies are less than 12 Gyr (see the right panel of Figure 8), so we do not have enough galaxies as old as NGC 4993.

3.4. Merge Events for Galaxies at Other Redshifts

The host galaxies of short-duration gamma-ray bursts (SGRBs) can be observed to larger redshifts. In Figures 10 and 11, we show the normalized probability of a BNS or BBH merger event P/P_{\max} in the $\log_{10}(M_*/M_{\odot})$ – $\log_{10}(\text{sSFR}/\text{yr}^{-1})$ plane for galaxies at different redshifts (i.e., $z = 0.1, 0.25, 0.5, 1.0, 2.0,$ and 3.0). The left panel of Figure 12 gives the normalized probability of a BNS merger event P as a function of $\log_{10}(\text{sSFR}/\text{yr}^{-1})$ for galaxies at different redshifts (i.e.,

$z = 0.1, 0.25, 0.5, 1.0, 2.0,$ and 3.0). The mean sSFR for galaxies with a given stellar mass increases with redshift (see Figure 5 in Moster et al. 2018), so P moves upwards with increasing redshift in Figure 10 and moves to the right in Figure 12. There exists a bimodal distribution at low redshifts as shown in the previous section. When $z > 1.0$, a unimodal distribution indicates that most galaxies are on the star formation main sequence (see Figure 12 and Figure 16 in Moster et al. 2020). Figure 11 is similar to Figure 10 but the BBH merger event has a larger dispersion on P .

4. Discussion

In this work, we use the linear $f_{\text{BBH}} - \log_{10}(Z/Z_{\odot})$ relation. The middle and right panels of Figure 8 show that, on average, the probability of a BBH merger is larger than that of a BNS merger,

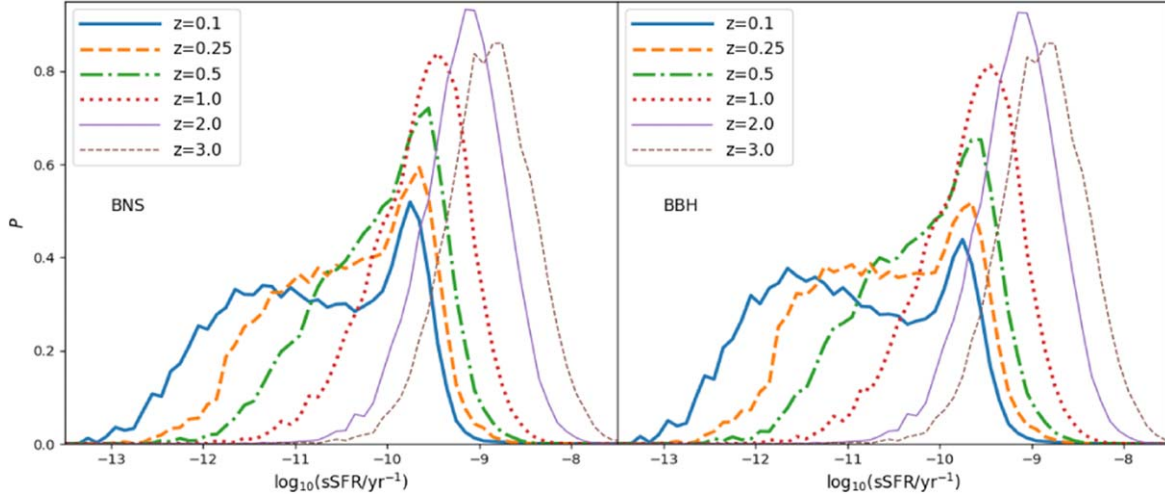


Figure 12. The normalized probability P of a BNS merger event (left) or a BBH merger event (right) as a function of $\log_{10}(\text{sSFR}/\text{yr}^{-1})$ for galaxies at different redshifts (i.e., $z = 0.1, 0.25, 0.5, 1.0, 2.0,$ and 3.0).

and both of them are dominated by low sSFR and old galaxies. The reason is that as the key parameter ζ decreases with Z , more BBHs are produced in a metal-poor SP. This difference in the probability between BBH and BNS mergers has arisen in the early universe, since the low sSFR and old galaxies have been formed in the low-metallicity environment. The normalized probability profiles of BBH and BNS mergers are similar (see Figures 7 and 8), and the parameter ζ has an insignificant effect on distinguishing them. With increasing metallicity, some other models predict that f_{BBH} drops more quickly than ours. These models can make this difference in the probability between BBH and BNS mergers become large.

In this work, we use $\eta = \text{const.}$ (i) If η increases with metallicity near $Z = Z_{\odot}$ as predicted by some studies, this would raise the probability of occurrence P for metal-rich galaxies, i.e., young and high sSFR galaxies, and lower the probability for quenched galaxies with low sSFR. This will lead to two peaks in the right panel of Figure 8 (P -Age) for the BNS merger, similar to Figure 9 of Jiang et al. (2020) ($P \sim 20\%$ at age = 7.0 Gyr, $\sim 5\%$ at age = 11.0 Gyr). The age of the quenched galaxies in the right panel of Figure 8 is 11 Gyr. The probability P for the quenched galaxies in this paper ($\eta = \text{const.}$) is the upper limit for the above studies (η increases with metallicity). (ii) If η decreases then increases with Z , for example, η reaches its minimum value near $Z = 0.1 Z_{\odot}$ as shown in the top panel of Figure 2 and Giacobbo & Mapelli (2019, by using the low efficiency of CE ejection, see Section 2.2.1), and the probability as a function of age is more complicated.

5. Summary

In this work, we build a parameterized phenomenological model of cosmic GW merger events to fit the observed

posterior sample for BBH events from GWTC-1, then study the probability of a BBH/BNS merger as functions of stellar mass, metallicity, sSFR, and age for galaxies with redshift $z \leq 0.1$ according to the best-fitting model. First, we utilize the BSE code to study the relation between the number of BBH/BNS mergers in an SP $f_{\text{BBH}}/f_{\text{BNS}}$ and metallicity. We find that f_{BBH} decreases linearly with metallicity. f_{BNS} does not vary with metallicity for most BPS calculations. So we assume that f_{BBH} has a negative correlation with the logarithm of metallicity within a certain range and f_{BNS} is invariant in this work. Second, using the maximum BH mass m_{max} by using BSE code and the B08 results, we present the functional form and the coefficient range for $m_{\text{max}}-Z$. Third, we obtain that the minimum BH mass is $7.9 M_{\odot}$, the maximum is $93_{-22}^{+73} M_{\odot}$, the exponent of the power function of the BBH mass-ratio distribution is $\beta = 13_{-6.12}^{+9.16}$, the slope of $f_{\text{BBH}} - \log_{10}(Z/Z_{\odot})$ is $\zeta = -8.32_{-4.38}^{+5.12}$, and the present-day mean metallicity is $0.4 Z_{\odot}$. Finally, by combining our results with the EMERGE empirical galaxy model, we show how the probability P of a merger event varies with the galaxy's stellar mass, sSFR, metallicity, and age.

The results are as follows. (i) the BBH mergers mostly happen in galaxies with $M_{*} = 10^{10.8} M_{\odot}$, which is similar to the previous work and the stellar mass of NGC 4993 ($4.46 \times 10^{10} M_{\odot}$). (ii) The quenched galaxies can produce a high proportion of BBH/BNS merger events in this work. There exist two peaks in the middle panel of Figure 8 ($P-\log_{10}(\text{sSFR}/\text{yr}^{-1})$), and the left one ($\log_{10}(\text{sSFR}/\text{yr}^{-1}) \sim -12$) stands for the contribution of the quenched galaxies. The sSFR value corresponding to the left peak is smaller than the previous results ($\log_{10}(\text{sSFR}/\text{yr}^{-1}) \sim -10$) and agrees with NGC 4993 ($\log_{10}(\text{sSFR}/\text{yr}^{-1}) = -12.65$). The left peak arises because the quenched galaxies at high redshift make a

large contribution to the total SFR in the empirical galaxy model as shown in Figure 9. (iii) The age at which the probability reaches the maximum is 11 Gyr. This value is greater than in previous studies (6–8 Gyr) and agrees with NGC 4993 (13.2 Gyr).

Our Bayesian method needs to be improved because it cannot fit the tail of the m_1 distribution extending to large mass. The distribution of the parameter ζ is slightly uncertain. More information about massive binary evolution or observed data needs to be obtained in the future. The host galaxy of GW170817 (NGC 4993) has a lower sSFR and greater age than the model results, so the empirical galaxy models need to be improved. If the delay times of BBH and BNS mergers have similar functional forms, the redshift distribution of short gamma-ray bursts can be reproduced by convolving the delay time with the cosmic SFR (Mandhai et al. 2022), which will help us improve the cosmic GW merger model. In the future, we will use the observed GW events and the redshift distribution of short gamma-ray bursts in our models.

Acknowledgments

This work is supported by the National Key R&D Program of China (No. 2021YFA1600403), the National Natural Science Foundation (NSF) of China (No. 11973081, 11573062, 11403092, 11390374, 11521303), the YIPACAS Foundation (No. 2012048), the Chinese Academy of Sciences (CAS, KJZD-EW-M06-01), the NSF of Yunnan Province (No. 2019FB006), the Basic Science Center project of the NSF of China (No. 12288102), the Science Research grants from the China Manned Space Project (No. CMS-CSST-2021-A08), the Youth Project of Western Light of CAS, and the International Centre of Supernovae, Yunnan Key Laboratory (No. 202302AN360001).

References

- Aasi, J., Abadie, J., Abbott, B. P., et al. 2015, *CQGra*, 32, 115012
- Abbott, B. P., Abbott, R., Abbott, T. D., et al. 2017, *PhRvL*, 119, 161101
- Abbott, B. P., Abbott, R., Abbott, T. D., et al. 2018, *LRR*, 21, 3
- Abbott, B. P., Abbott, R., Abbott, T. D., et al. 2019a, *ApJL*, 882, L24
- Abbott, B. P., Abbott, R., Abbott, T. D., et al. 2019b, *PhRvX*, 9, 031040
- Abbott, B. P., Abbott, R., Abbott, T. D., et al. 2020a, *ApJL*, 892, L3
- Abbott, R., Abbott, T. D., Abraham, S., et al. 2020b, *ApJL*, 896, L44
- Abbott, R., Abbott, T. D., Acernese, F., et al. 2021, arXiv:2111.03606
- Acernese, F., Agathos, M., Agatsuma, K., et al. 2015, *CQGra*, 32, 024001
- Artale, M. C., Mapelli, M., Bouffanais, Y., et al. 2020, *MNRAS*, 491, 3419
- Artale, M. C., Mapelli, M., Giacobbo, N., et al. 2019, *MNRAS*, 487, 1675
- Banerjee, S., Belczynski, K., Fryer, C. L., et al. 2020, *A&A*, 639, A41
- Belczynski, K., Askar, A., Arca-Sedda, M., et al. 2018, *A&A*, 615, A91
- Belczynski, K., Bulik, T., Fryer, C. L., et al. 2010, *ApJ*, 714, 1217
- Belczynski, K., Heger, A., Gladysz, W., et al. 2016a, *A&A*, 594, A97
- Belczynski, K., Holz, D. E., Bulik, T., & O’Shaughnessy, R. 2016b, *Natur*, 534, 512
- Belczynski, K., Kalogera, V., & Bulik, T. 2002, *ApJ*, 572, 407
- Belczynski, K., Kalogera, V., Rasio, F. A., et al. 2008, *ApJS*, 174, 223
- Blanchard, P. K., Berger, E., Fong, W., et al. 2017, *ApJL*, 848, L22
- Boersma, O. M., van Leeuwen, J., Adams, E. A. K., et al. 2021, *A&A*, 650, A131
- Bray, J. C., & Eldridge, J. J. 2016, *MNRAS*, 461, 3747
- Buchner, J., Georgakakis, A., Nandra, K., et al. 2014, *A&A*, 564, A125
- Chan, C., Müller, B., Heger, A., Pakmor, R., & Springel, V. 2018, *ApJL*, 852, L19
- Chruslinska, M., Belczynski, K., Klencki, J., & Benacquista, M. 2018, *MNRAS*, 474, 2937
- Chruslinska, M., & Nelemans, G. 2019, *MNRAS*, 488, 5300
- Chu, Q., Yu, S., & Lu, Y. 2022, *MNRAS*, 509, 1557
- Dewi, J. D. M., Podsiadlowski, P., & Pols, O. R. 2005, *MNRAS*, 363, L71
- Dvorkin, I., Vangioni, E., Silk, J., Uzan, J.-P., & Olive, K. A. 2016, *MNRAS*, 461, 3877
- Eldridge, J. J., & Tout, C. A. 2004, *MNRAS*, 353, 87
- Farr, W. M., Sravan, N., Cantrell, A., et al. 2011, *ApJ*, 741, 103
- Feroz, F., Hobson, M. P., & Bridges, M. 2009, *MNRAS*, 398, 1601
- Fishbach, M., Essick, R., & Holz, D. E. 2020, *ApJL*, 899, L8
- Fishbach, M., Holz, D. E., & Farr, W. M. 2018, *ApJL*, 863, L41
- Fryer, C. L., Belczynski, K., Wiktorowicz, G., et al. 2012, *ApJ*, 749, 91
- Giacobbo, N., & Mapelli, M. 2018, *MNRAS*, 480, 2011
- Giacobbo, N., & Mapelli, M. 2019, *MNRAS*, 482, 2234
- Giacobbo, N., Mapelli, M., & Spera, M. 2018, *MNRAS*, 474, 2959
- Gormaz-Matamala, A. C., Curé, M., Meynet, G., et al. 2022, *A&A*, 665, A133
- Hannam, M., Schmidt, P., Bohé, A., et al. 2014, *PhRvL*, 113, 151101
- Hansen, B. M. S., & Phinney, E. S. 1997, *MNRAS*, 291, 569
- Hobbs, G., Lorimer, D. R., Lyne, A. G., & Kramer, M. 2005, *MNRAS*, 360, 974
- Hurley, J. R., Pols, O. R., & Tout, C. A. 2000, *MNRAS*, 315, 543
- Hurley, J. R., Tout, C. A., & Pols, O. R. 2002, *MNRAS*, 329, 897
- Husa, S., Khan, S., Hannam, M., et al. 2016, *PhRvD*, 93, 044006
- Ivanova, N., & Nandez, J. L. A. 2016, *MNRAS*, 462, 362
- Jiang, Z., Wang, J., Zhang, F., et al. 2020, *MNRAS*, 498, 926
- Khan, S., Husa, S., Hannam, M., et al. 2016, *PhRvD*, 93, 044007
- Kovetz, E. D., Cholis, I., Breyse, P. C., & Kamionkowski, M. 2017, *PhRvD*, 95, 103010
- Kroupa, P., Tout, C. A., & Gilmore, G. 1993, *MNRAS*, 262, 545
- Kuroda, T., Fischer, T., Takiwaki, T., & Kotake, K. 2022, *ApJ*, 924, 38
- Kuroda, T., Kotake, K., Takiwaki, T., & Thielemann, F.-K. 2018, *MNRAS*, 477, L80
- Lau, M. Y. M., Hirai, R., González-Bolívar, M., et al. 2022, *MNRAS*, 512, 5462
- Levan, A. J., Lyman, J. D., Tanvir, N. R., et al. 2017, *ApJL*, 848, L28
- Littenberg, T. B., Farr, B., Coughlin, S., Kalogera, V., & Holz, D. E. 2015, *ApJL*, 807, L24
- Madau, P., & Dickinson, M. 2014, *ARA&A*, 52, 415
- Mandhai, S., Lamb, G. P., Tanvir, N. R., et al. 2022, *MNRAS*, 514, 2716
- Mapelli, M., Giacobbo, N., Ripamonti, E., & Spera, M. 2017, *MNRAS*, 472, 2422
- Mapelli, M., Giacobbo, N., Toffano, M., et al. 2018, *MNRAS*, 481, 5324
- Molero, M., Simonetti, P., Matteucci, F., & della Valle, M. 2021, *MNRAS*, 500, 1071
- Moster, B. P., Naab, T., & White, S. D. M. 2018, *MNRAS*, 477, 1822
- Moster, B. P., Naab, T., & White, S. D. M. 2020, *MNRAS*, 499, 4748
- Özel, F., Psaltis, D., Narayan, R., & McClintock, J. E. 2010, *ApJ*, 725, 1918
- Palmese, A., Hartley, W., Tarsitano, F., et al. 2017, *ApJL*, 849, L34
- Planck Collaboration, Ade, P. A. R., Aghanim, N., et al. 2016, *A&A*, 594, A13
- Podsiadlowski, P., Langer, N., Poelarends, A. J. T., et al. 2004, *ApJ*, 612, 1044
- Raaijmakers, G., Nisanke, S., Foucart, F., et al. 2021, *ApJ*, 922, 269
- Rastello, S., Amaro-Seoane, P., Arca-Sedda, M., et al. 2019, *MNRAS*, 483, 1233
- Ricker, P. M., & Taam, R. E. 2008, *ApJL*, 672, L41
- Safarzadeh, M., & Farr, W. M. 2019, *ApJL*, 883, L24
- Salim, S., Rich, R. M., Charlot, S., et al. 2007, *ApJS*, 173, 267
- Santoliquido, F., Mapelli, M., Artale, M. C., & Boco, L. 2022, *MNRAS*, 516, 3297
- Santoliquido, F., Mapelli, M., Giacobbo, N., Bouffanais, Y., & Artale, M. C. 2021, *MNRAS*, 502, 4877
- Simonetti, P., Matteucci, F., Greggio, L., & Cescutti, G. 2019, *MNRAS*, 486, 2896
- Springel, V. 2005, *MNRAS*, 364, 1105
- Talbot, C., & Thrane, E. 2018, *ApJ*, 856, 173
- Tauris, T. M., Kramer, M., Freire, P. C. C., et al. 2017, *ApJ*, 846, 170
- Trani, A. A., Rieder, S., Tanikawa, A., et al. 2022, *PhRvD*, 106, 043014
- Vangioni, E., Olive, K. A., Prestegard, T., et al. 2015, *MNRAS*, 447, 2575
- Vartanyan, D., Coleman, M. S. B., & Burrows, A. 2022, *MNRAS*, 510, 4689
- Vink, J. S., & Sander, A. A. C. 2021, *MNRAS*, 504, 2051
- Wetzel, A. R., Tinker, J. L., & Conroy, C. 2012, *MNRAS*, 424, 232